

Simulation and analysis of intervention costs due to wind-induced damage on tall buildings



Wei Cui, Luca Caracoglia *

Department of Civil and Environmental Engineering, Northeastern University, Boston, MA 02115, USA

ARTICLE INFO

Article history:

Received 15 June 2014

Revised 28 November 2014

Accepted 1 January 2015

Available online 11 February 2015

Keywords:

Tall buildings

Wind loading

Fragility analysis

Life-cycle cost estimation

Performance-based engineering

CAARC building

ABSTRACT

A numerical algorithm is developed for estimating the life-cycle monetary losses (maintenance and repair costs) due to wind-induced damage on tall buildings. The wind loading on tall buildings is evaluated by combining the effect of buffeting forces and vortex shedding forces. The translation process theory is subsequently used to estimate the peak value of the resultant response, which is a non-Gaussian stochastic process. “Fragility curves”, accounting for random aerodynamic coefficients due to experimental errors, are used to estimate vulnerability and wind-induced damage probability. These curves represent the probability of exceeding a given structural damage state (or performance threshold), conditional on the mean wind speed. The thresholds are based on top-floor resultant acceleration, for occupant comfort, and resultant peak displacements, for structural damage. The results of the fragility analysis and wind speed probability are subsequently used to analyze monetary losses. The cost analysis model is adapted from an existing life-cycle simulation algorithm for earthquake hazards.

The pilot study employs a 183 m tall building (CAARC model). Fragility and life-time cost analysis simulate the behavior of a building located in a “mixed” wind climate, typical of Southern Florida in the United States. Effects of various limit state criteria, meteorological environment and measurement accuracy of the structural parameters are discussed.

© 2015 Elsevier Ltd. All rights reserved.

1. Introduction

1.1. Context and methods: performance-based engineering

Over the past several years, performance-based engineering (PBE) has been developed and applied by structural engineers and researchers in seismic engineering. For instance, the Structural Engineers Association of California has set about a framework for the design of structures, based on the correspondence between earthquake recurrence intervals and performance levels [1], in which performance levels are combined with earthquake excitation levels to determine appropriate design criteria. The basic concept is to ensure the structure to satisfy the selected performance requirement, when subjected to different levels of the hazard, in order to achieve performance-based design [2]. The next important and logical step is to apply this advanced procedure to the wind

engineering field and to evaluate the performance of either new or existing structures under wind load [3].

The derivation of more rational performance-based design methods has received the attention of the research community, as indicated by the numerous studies in recent years on this subject [4–10]. The fundamental idea behind PBE is to “expand” the flexibility of the design procedure [11]. It is to ensure that a building, for example, subjected to different levels of a hazard (as opposed to the largest foreseeable event), is capable of achieving a selected performance objective level [12]. Current PBE methodologies go beyond the prescriptive specifications of a design standard by ensuring that life safety is preserved under “severe” events. They also establish criteria for the structure not to collapse under “extreme” events, and to preserve immediate occupancy under “moderate” events. Interestingly, the exact definitions of “severe”, “extreme”, and “moderate” are still under development [12]. The overall concept of PBE provides an attractive alternative for owners, since it can enable cost-effective design and can reduce planning in the aftermath of a catastrophic event.

A brief literature review of PBE in the wind engineering field has revealed that most attention has been given to the study of the load effects on low-rise buildings [12–16], where damage and

* Corresponding author at: Department of Civil and Environmental Engineering, Northeastern University, 400 Snell Engineering Center, 360 Huntington Avenue, Boston, MA 02115, USA. Tel.: +1 617 373 5186; fax: +1 617 373 4419.

E-mail address: lucac@coe.neu.edu (L. Caracoglia).

Nomenclature

B	building width	$\bar{U}(z)$	mean wind speed at height z
B_w	spectral bandwidth	u	wind turbulence in along-wind direction
$C(t)$	total cost at time t	u^*	shear flow velocity
C_0	initial cost of the structure	v	wind turbulence in crosswind direction
C_D	drag coefficient	\bar{X}	mean static displacement
C_L	lift coefficient	z_0	roughness length of boundary layer
C_j	repair cost for exceeding the limit state j at present monetary value	$\zeta_{a,i}$	aerodynamic damping for direction i
C_{zi}	decay coefficient of the co-coherence function for turbulence in direction i	$\zeta_{s,i}$	structural damping for direction i
\tilde{C}_L	RMS lift coefficient	κ	average occurrence parameter of Poisson process $N(t)$
D	building depth	λ	discount rate per year
$F()$	cumulative distribution function	μ_i	expectation of variable i
F_{T_j}	fragility curve for limit state j	v	up-crossing rate
$f()$	probability distribution function	ρ	air density
g	peak effect factor	σ_i	standard deviation (RMS) of variable i
h	building height	$\Phi_i(z)$	shape function along direction i
I_u	turbulence intensity		
k	total number of limit states considered	Subscripts	
L_s	vortex shedding correlation length	H	hurricane climate
$M_{g,i}$	generalized mass for fundamental mode along direction i	j	j -th limit state
$N(t)$	total number of wind hazards at time t	m	mixed climates
n	frequency	NH	non-hurricane climate
n_s	frequency of vortex shedding	r	resultant response
$n_{0,i}$	fundamental natural frequency for direction i	\ddot{x}	along-wind motion acceleration
$P[]$	probability operator	\dot{x}	along-wind motion velocity
P_j	annual probability of exceeding the limit state j	x	along-wind direction
S_{ii}	power spectral density of random variable i	\dot{y}	crosswind motion acceleration
t	time (in years, for cost analysis)	y	crosswind motion velocity
		y	crosswind direction

collapse can be related to localized loss of capacity in key members or connections. Few studies are available on high-rise buildings, in which either a framework for the analysis of uncertainty is developed [17], or in which a methodology for the design of buildings is proposed [18,19]. Some attention has been recently paid to wind loads on long-span bridges [20,21].

1.2. Motivation of the study in the context of wind load analysis on tall buildings

From the early stages of the research activities on tall buildings in wind engineering, the frequency domain analysis method has been employed due to the presence of random turbulent wind and consequent structural random vibration [22,23]. The evaluation of the dynamic response of tall buildings accounts for two main phenomena: buffeting and vortex shedding. Buffeting is an aerodynamic phenomenon, caused by the interaction between wind turbulence and the structure in motion. The dynamic motion caused by buffeting loads can be adequately predicted under quasi-static loading assumption, in which all aerodynamic load parameters are assumed as constant and measured by a number of static force coefficients averaged over time. In general, buffeting force will increase with the mean wind speed. Vortex shedding is a periodic loading mechanism at a predominant frequency that occurs when wind flows around a bluff body at given speed. For flexible structures, such as very tall and flexible buildings of the new generation, it is conceivable that the frequency of vortex shedding, which depends on the size and shape of the structure, may approach the fundamental frequency of the structure, possibly causing large-amplitude vibration at certain wind speeds [24].

In PBE fragility curves are often used to evaluate the probability of a system reaching or exceeding a limit state as a function of the hazard intensity (engineering demand), such as the peak ground acceleration or the mean wind speed at a predefined height from the ground in high winds. Originally developed in earthquake engineering, they have become a very useful tool to evaluate structural integrity for performance-based design. In the case of wind engineering the method can account for various sources of uncertainty including error-contaminated aerodynamic parameters. Recently, in parallel with the development of computer technology, Monte-Carlo simulation has become an important numerical approach for generating fragility curves [18] on computer clusters as well as on general purpose graphic processing unit (GPGPU) [25]. As a result, fragility analysis, based on Monte Carlo simulation, has been recently investigated in wind engineering and successfully applied to tall buildings [2] and long-span bridges [21].

This study will focus on the uncertainty associated with unavoidable experimental errors in a wind tunnel test, used to determine the loads on the full-scale structure; it has been shown that this can be a relevant uncertainty source for structural reliability [2,21,26]. For instance, experiments conducted on the same building model in different laboratories can lead to different results due to different geometric scales in the models or variations in the properties of the boundary layer replicated in the wind tunnel [27]. These aspects lead to an inherent variability in the aerodynamic load coefficients, confirming the stochastic nature of the aerodynamic parameters. This study aims at specifically examining the relevance of this uncertainty type on the predicted response of a tall building. It is clear that other relevant uncertainty sources should be considered in future studies. Other uncertainty sources may include: test facilities, human errors, test procedures, wind

patterns, frequency content of wind loading, slowly-varying wind speed fluctuations over time inducing non-stationary loads and vibration. Nevertheless, these have not been considered herein since the main objective was the development of a “simulation framework” for risk analysis, in which the role of costs is directly employed to analyze life-cycle structural performance.

Tall buildings, being the land-mark and center of human activities, greatly influence local culture, economics, and other aspects of society. Therefore, monetary cost is a very important factor in tall building design besides structural safety. Recently, life-cycle cost analysis has been recognized as an innovative methodology to examine performance of structures and facilities, taking into account cost of construction, maintenance, repair and demolition. The advancement of probabilistic methods enables engineers to treat both the natural hazards and the limit states being exceeded as random process during the life-time of the structure [28]. This methodology has been implemented and applied to reinforced concrete structures [29], highway bridges [30] and long-span bridges [21].

Nevertheless, very few examples of life-cycle cost analysis due to wind-induced damage on tall buildings are available due to the difficulty of “technology transfer” from other fields (e.g., earthquake engineering) and the uniqueness of the wind turbulence excitation mechanism [2]. This study will apply the methodology for estimating intervention costs (maintenance and repair) to the life-cycle analysis of a 183 m tall building, based on wind speed recurrence probability and fragility analysis, which accounts for experimental errors. Finally, it must be noted that a more realistic classification of the limit states should rely on economic analysis of current construction costs and should include a more detailed study on other damaging and failure modes for the building components; this aspect is not directly investigated in this study but will be part of future research activities.

2. Background theory

2.1. Frequency domain analysis in the along-wind and cross-wind directions

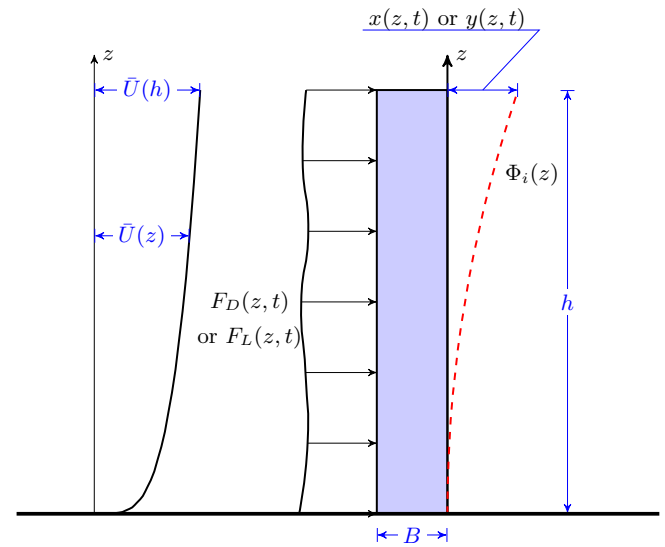
Standard frequency domain random vibration analysis has been traditionally utilized for the estimation of the wind-induced loading and dynamic response of tall buildings [22,23,31].

The building is modeled as a slender prismatic cantilever structure with a rectangular floor-plan section, which is symmetrical to both (strong and weak) axes of bending. The mean wind direction coincides with direction “x” in Fig. 1(b) and is perpendicular to one of the vertical faces of the structure. Due to the geometric symmetry and loading planes, torsional effects are ignored at this time; moreover, only the first fundamental modes in the along-wind and crosswind directions are considered in this investigation. From quasi-static theory [22,32], PSD (power spectral density) of the generalized buffeting force can be determined as in Eq. (1) for the along-wind direction and in Eq. (2) for the crosswind direction.

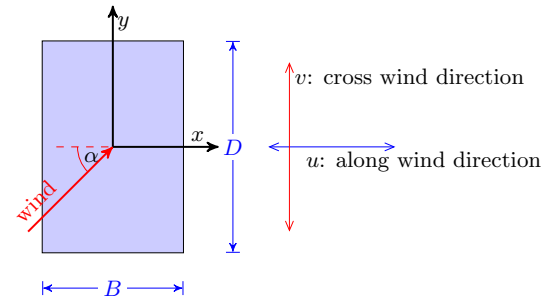
$$S_{Q_x Q_x}(n) = \iint_h C_D^2 \rho^2 D^2 \Phi_x(z_1) \Phi_x(z_2) \bar{U}(z_1) \bar{U}(z_2) S_{uu}(n, z_1, z_2) dz_1 dz_2 \quad (1)$$

$$S_{Q_{b_y} Q_{b_y}}(n) = \iint_h \left[C_L^2 S_{vv}(n, z_1, z_2) + \frac{1}{4} \left(\frac{\partial C_L}{\partial \alpha} + C_D \right)^2 S_{uu}(n, z_1, z_2) \right] \times \rho^2 D^2 \Phi_y(z_1) \Phi_y(z_2) \bar{U}(z_1) \bar{U}(z_2) dz_1 dz_2 \quad (2)$$

In the previous equations ρ is the air density, $\Phi_x(z)$, $\Phi_y(z)$ are mode shape functions in along-wind direction and crosswind direction, $\bar{U}(z)$ is the mean wind velocity at height z , D is a refer-



(a) Lateral view of tall building



(b) horizontal plane and wind directionality

Fig. 1. Schematic of tall building and wind directionality. α : relative wind direction.

ence dimension (width of building, see Figs. 1(b) and 3, C_D is the drag coefficient, C_L is the lift coefficient, and $\frac{\partial C_L}{\partial \alpha}$ is the derivative of C_L with respect to wind direction α .

From the frequency domain theory, the PSD of building response can be directly calculated from the PSD of dynamic force, as shown in Eq. (3),

$$S_{xx}(z_1, z_2, n) = \frac{\Phi_x(z_1) \Phi_x(z_2) S_{Q_x Q_x}}{16\pi^2 M_{g,x}^2 \left[(n_{0,x}^2 - n^2)^2 + [2nn_{0,x}(\zeta_{s,x} + \zeta_{a,x})]^2 \right]} \quad (3)$$

in which $n_{0,x}$ is the structural natural frequency for x direction, $M_{g,x}$ is the generalized mass derived from mode shape function $\Phi_x(z)$ and $\zeta_{s,x}$, $\zeta_{a,x}$ are structural damping and aeroelastic damping for x direction respectively. In the cross-wind direction, vortex-induced vibration may occur when vortices are shed alternately in the wake of the building [33]. Because of the effect of the vortex shedding, the lift force coefficient can be considered as a stochastic Gaussian process $C_L(t)$ with a zero mean rather than a constant term.

From [33], the auto-spectrum of the lift coefficient fluctuation due to vortex shedding $S_{C_L}(z, n)$ using Eq. (4) [34] is expressed as:

$$\frac{n S_{C_L}(z, n)}{\tilde{C}_L^2(z)} = \frac{n}{\sqrt{\pi} B_w(z) n_s(z)} \exp \left[- \left(\frac{1 - \frac{n}{n_s(z)}}{B_w(z)} \right)^2 \right] \quad (4)$$

where \tilde{C}_L is the standard deviation of the vortex shedding lift coefficient C_L ; n_s is the frequency of vortices, $n_s = S_t D / \bar{U}(h)$; S_t is the Strouhal number; B_w is the band width.

For vortex shedding, it is sufficiently accurate to use the correlation length [33] to simplify the generalized force:

$$S_{Q_{vry}Q_{vry}}(n) = \frac{2L_s}{\sqrt{\pi}n_{0,y}} \times \int_0^h \left(\frac{1}{2} \rho \bar{U}^2(z) D \tilde{C}_L \Phi_y(z_1) \right)^2 \frac{n}{B_w(z)n_s(z)} \times \exp \left[- \left(\frac{1 - \frac{n}{n_s(z)}}{B_w(z)} \right)^2 \right] dz \quad (5)$$

in which L_s stands for correlation length and D is the building dimension defined above. Based on the assumption that the crosswind buffeting forces and vortex shedding loads can be considered as mutually independent [35], the PSD of the crosswind dynamic response can be derived according to Eq. (6).

$$S_{yy}(z_1, z_2, n) = \frac{\Phi_y(z_1)\Phi_y(z_2)(S_{Q_{by}Q_{by}} + S_{Q_{vry}Q_{vry}})}{16\pi^2 M_{gy}^2 \left[(n_{0,y}^2 - n^2)^2 + [2nn_{0,y}(\zeta_{s,y} + \zeta_{a,y})]^2 \right]} \quad (6)$$

At last, the evaluation of RMS (root mean square) top-floor lateral displacement and acceleration of the building (at $z = h$) can be found by converting the one-sided PSD of the response to RMS values in Eq. (7):

$$\sigma_i(z) = \sqrt{\int_0^\infty S_{ii}(z, z, n) dn} \quad \sigma_i = 4\pi^2 \sqrt{\int_0^\infty n^4 S_{ii}(z, z, n) dn} \quad (7)$$

in which i could be x or y .

2.2. Peak response estimation

In wind engineering, peak response can be calculated from the theory in [36,37]. However, in the case of the resultant response $r(t)$ (either resultant displacement or acceleration) as in Eq. (8) below, which combines the components from both along-wind and crosswind directions rather than the response along a single principal direction, the Gaussian process is no longer an adequate model for the resultant response [38,39].

$$r(t) = \sqrt{r_x^2(t) + r_y^2(t)} \quad (8)$$

In order to estimate the extreme-value expectation of a non-Gaussian process, several models have been proposed, such as the translation process model [40], the Hermite moment model [41] and the vector process model [42]. Moreover, some simplified methods either using the square-root-of-sum-square (SRSS) rule or the complete-quadratic-combination (CQC) rule have been employed in wind engineering research for tall buildings [43].

2.3. Fragility analysis

The objective of a fragility analysis is the computation of the conditional probability that a representative structural response parameter (maximum lateral drift, RMS acceleration, etc.), corresponding to a specific feature of the dynamic response [2], exceeds a pre-selected threshold. The set of thresholds is usually defined by the designer to describe different structural performance requirements. In this paper, the exceedance probabilities are estimated using the numerical method described in [2,20].

Selection of the thresholds should illustrate the building performance requirement against the wind hazards. Generally, the main concern of the designer against wind loads is not related to the strength limit state of the tall building. For serviceability limit states, which are defined as functional performance under the load and include items such as deflection and vibration, the designer mostly focuses on two important aspects: lateral drift and motion perception (acceleration). For example, excessive lateral drift may

damage the cladding system (windows cracking or distortion), the electrical system and water supply system. Large acceleration can cause occupant discomfort and damage to sensitive instruments. All these possible damages will require extra maintenance, repair and replacement during building lifetime. For serviceability, according to [8], $h/400$ can be selected as the limit state threshold for maximum lateral drift of the roof. For the motion perception–acceleration threshold, the use of peak acceleration or RMS acceleration has been debated for in academia. But, as explained in [44], the RMS quantity is better correlated to human response symptoms and also much simpler to numerically evaluate. As a result, in this study, 5 mg RMS acceleration is chosen as the threshold for the motion perception limit state [8,45].

In the fragility analysis, another important factor is the selection of input random variables. In Eqs. (1) and (2), C_D and $\frac{\partial C_L}{\partial \alpha}$ are two important coefficients, which relate the wind speed to wind pressure loads on the structure. Moreover, these two quantities are usually measured indirectly from a wind tunnel test, which suggests that C_D and $\frac{\partial C_L}{\partial \alpha}$ can be contaminated by many errors (measurement fidelity, model fabrication, digital signal acquisition, etc.). Similarly, for vortex shedding in Eq. (5), \tilde{C}_L is also usually experimentally found and can be another source of uncertainty. From [2,20], it has been noted that the gamma-type distribution can be used to adequately represent the variability in the aerodynamic coefficients C_D and \tilde{C}_L . The normal distribution is adopted to simulate the random coefficient $\frac{\partial C_L}{\partial \alpha}$. Therefore, the numerical evaluation of fragility in this paper will include three random variables: C_D , $\frac{\partial C_L}{\partial \alpha}$ and \tilde{C}_L .

2.4. Annual maxima of wind speed

Assessment of life-time cost needs the estimation of occurrence possibility of the hazard [28]. In wind engineering, the largest annual mean wind speed distribution model is required. In a non-hurricane-prone region of the United States, the largest annual wind speed can be well modeled by a Type I extreme value distribution (Gumbel distribution) [37,46,47]. However, in hurricane-prone regions, the local climate is subjected to both hurricanes and synoptic winds; therefore the traditional Gumbel model may underestimate the probability of high winds related to hurricane landfall.

Thus, a more accurate probability model using a mixed distribution was recommended in [37,46,48] and is adopted in several design standards [49]. The cumulative distribution function (CDF) of the mixed distribution is estimated as [37,46]

$$F_m(V_E \leq V) = F_H(V_E \leq V)F_{NH}(V_E \leq V) \quad (9)$$

where $F_m(V_E \leq V)$ is the probability that the wind speed V_E , associated with any storm is less than or equal to a given value V in any one year, and $F_H(V_E \leq V)$ and $F_{NH}(V_E \leq V)$ are the probabilities that hurricane wind speeds (H) and non-hurricane wind speeds (NH) are less than or equal to V in any one year. This equation is based on the assumption that occurrence of hurricane winds and occurrence of non-hurricane winds are independent [37,46]. As a result, the PDF of the mixed distribution can be derived from Eq. (9) as

$$f_m(V) = \frac{dF(V_E \leq V)}{dV} = f_{NH}(V)F_H(V_E \leq V) + f_H(V)F_{NH}(V_E \leq V) \quad (10)$$

in which $f_m(V)$, $f_H(V)$ and $f_{NH}(V)$ are PDFs for mixed wind speeds, hurricane wind speeds and non-hurricane wind speeds respectively.

In Eqs. (9) and (10), the probability model for hurricane landfall along the south-east coastline of the United States can be efficiently simulated by Monte Carlo method [50,51]. As shown in [37,50] the Type III extreme value distribution (Weibull) can be utilized to model the coastline hurricane wind speeds generated by Monte Carlo simulation.

2.5. Estimation of life-time monetary losses

The algorithm for life-cycle cost analysis makes use of the fragility analysis result (fragility curves) to predict damage-induced monetary losses over a time period (t , unit: year) which may be the design life of a new structure or the remaining life of a retrofitted structure. The expected total cost $C(t)$ can be expressed as a function of t as follows [28]:

$$E[C(t)] = C_0 + E \left[\sum_{i=1}^{N(t)} \sum_{j=1}^k C_j e^{-\lambda t_i} P_j \right] \quad (11)$$

In the above equation, $E[\cdot]$ denotes expected value; C_0 is the initial construction cost of the structure; i is a number indexing the occurrence of the hazards over the structural life; t_i is the time at which i -th hazard occurs, which is a random variable; $N(t)$ is the total number of hazard occurrences over time t , which is assumed to be a Poisson process with average occurrence rate κ ; j is the index used to designate the different limit states; k is the total number of limit states considered in design; C_j is the intervention cost in present dollar value of the j -th limit state being reached at time t_i ; $e^{-\lambda t_i}$ includes the discount factor of C_j at time t_i ; λ is a constant discount rate per year; P_j is the probability of j -th limit state being reached, which means that the structure is damaged and needs repair, after each hazard. The previous equation does not include scheduled maintenance costs (e.g., aging of the cladding), unaffected by hazard and damage occurrence.

When estimating the life-time intervention cost for a building structure, Eq. (11) can be simplified to obtain the relative intervention costs $C_{M,E}$, which is the expected value of maintenance and repair costs normalized with respect to the initial construction cost C_0 [21], as

$$C_{M,E} = E \left[\frac{C(t) - C_0}{C_0} \right] = E \left[\sum_{i=1}^{N(t)} \sum_{j=1}^k \epsilon_j e^{-\lambda t_i} P_j \right] \quad (12)$$

where ϵ_j is the ratio of the intervention cost for the j -th limit state relative to the initial construction cost C_0 , so $\epsilon_j = C_j/C_0$.

As discussed in a previous section, the analysis of performance of a tall building against high winds, two limit states, lateral deformation (drift) and acceleration, can usually be considered. Therefore in Eq. (12) $k=2$ is employed; $j=1$ is used to designate the deformation limit state and $j=2$ denotes the acceleration limit state.

3. Proposed methodology for cost estimation

In Eqs. (12) and (11), P_j stands for the probability of exceedance of j -th limit states in any one year. From the combined structural fragility and local largest annual wind distribution, P_j is derived by the convolution integral in Eq. (13)

$$P_j = \int_0^\infty F_{T_j}(V_z) f_m(V_z) dV_z = \int_0^\infty P[Z > T_j | V_z = \bar{U}] f_m(V_z) dV_z \quad (13)$$

Therefore, the prediction of life-time monetary loss has a total of three steps:

- Step (1) Evaluation of fragility curve for each limit state F_{T_j} from frequency domain analysis, and subsequently, peak response estimation.
- Step (2) Modeling of annual maxima wind speed probability distribution $f_m(V_z)$ for combined hurricane and non-hurricane wind hazards in mixed wind climate region of the United States.
- Step (3) Monetary loss prediction over structural life-time with appropriate parameters and convolution integral, resulting in the probability P_j .

The entire process is summarized in the flow chart, shown in Fig. 2.

In the next section, an example of application of this analysis methodology will be illustrated.

4. Application of life-time cost methodology

4.1. Description of the simulated building

The CAARC building is selected since it has been used as a standard model for comparison among experimental data and analysis techniques, employed by various wind tunnels all over the world [27]. Fig. 3 shows a schematic view of the CAARC building with an indication of the main dimensions (depth D , width B , height h).

This building is a slender prismatic structure with a rectangular floor plan, which is symmetric with respect to both (strong and weak) axes of bending. The mass is assumed distributed uniformly along the building. Also, as stated in Ref. [31], high order modes are ignored in this study. Tables 1 and 2 summarize the CAARC building full-scale model parameters and the corresponding wind field parameters. The mean wind speed direction is assumed as orthogonal to the vertical face of dimension D .

Although the turbulence spectrum, needed by Eqs. (1) and (2) to calculate the generalized force PSD, was displayed in [27], the turbulence PSD function was only available at $z = \frac{2}{3}h$. Also, data on the crosswind turbulence component PSD were not presented in [27]. As a result, in this study Kaimal's Model is employed [52] to replicate the turbulence PSD function in [27]:

$$\frac{nS_u(z; n)}{u_*^2} = \frac{105f}{(1 + 33f)^{\frac{5}{3}}} \quad (14)$$

$$\frac{nS_v(z; n)}{u_*^2} = \frac{17f}{(1 + 9.5f)^{\frac{5}{3}}} \quad (15)$$

where $f = nz/\bar{U}(z)$ is the Monin coordinate.

In Table 1, the standard deviation of lift coefficient \bar{C}_L , the Strouhal number S_L and the correlation length L_s are derived according to the method described in [53] to simulate vortex shedding effects. The derivative of C_L with respect to the attack angle is calculated from [5]. The decay coefficients of the co-coherence function are taken as: $C_{zu} = 12$ [33] and $C_{zv} = 0.667C_{zu}$ [37].

4.2. Closed-form verification and preliminary investigations

The “closed-form” (CF) dynamic response solution is compared to wind tunnel based reference values from [27]. The CF computation uses a standard algorithm for calculation of the PSD in Eqs. (14) and (15), where recursive adaptive Simpson quadrature is employed.

An example of the results is shown in Fig. 4(a), where the CF numerical solution of the RMS and mean response in the along-wind direction are compared to wind tunnel experiments results in [27], as a function of the reduced velocity, $\bar{U}(h)/n_0D$. The building along-wind response is normalized with respect to the building

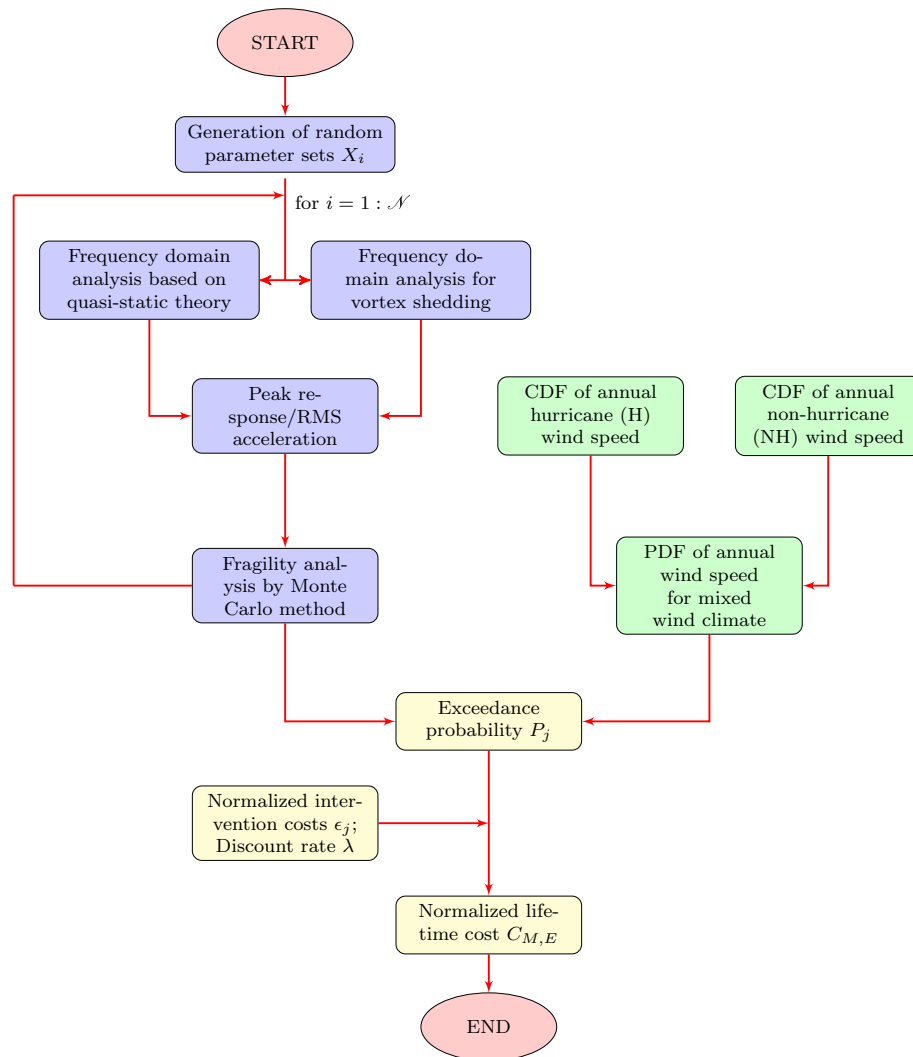


Fig. 2. Flow chart of structural life-time cost estimation methodology.

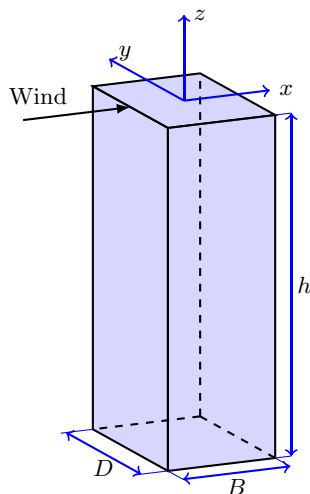


Fig. 3. Schematic view of the CAARC building.

width B . The curves in Fig. 4 are plotted using “spline interpolation” (C^2 continuity) to connect simulated points. Similarly, in Fig. 4(b), the CF numerical results in crosswind direction are com-

Table 1
Structural parameters.

Quantity	Value assigned
B	30.5 m
D	45.7 m
h	183 m
$m(z)$	223224.4 kg/m
$\zeta_{s,x}$	0.01
$n_{0,x} \ n_{0,y}$ (Hz)	0.2
$\Phi_x(z)$	$(z/h)^\gamma$; $\gamma = 1$
C_D	1.54
C_L	0
$\partial C_L / \partial \alpha$	-3.50
\tilde{C}_L	0.287
S_t	0.116
L_s	$1.5 \times B$

pared to test results. Excellent correspondence can be found in all three curves, which is the evidence of verification of the reference numerical model built in above section.

4.3. Investigation of resultant response

In structural design, resultant response induced by wind, simultaneously taking into account along-wind, crosswind and torsion,

Table 2
Wind field parameters.

Quantity	Value assigned
ρ	1.25 kg/m ³
Roughness, z_0	0.5 m
$\bar{U}(z)$ (m/s)	$\bar{U}(h)(z/h)^{0.28}$
$\bar{U}(h)$	0–50 m/s
u^*	$\bar{U}(h) / (2.5 \ln \frac{h}{z_0})$
I_u	$0.53 / (\ln \frac{h}{z_0})$
C_{zu}	12
C_{zv}	$0.667 C_{zu}$

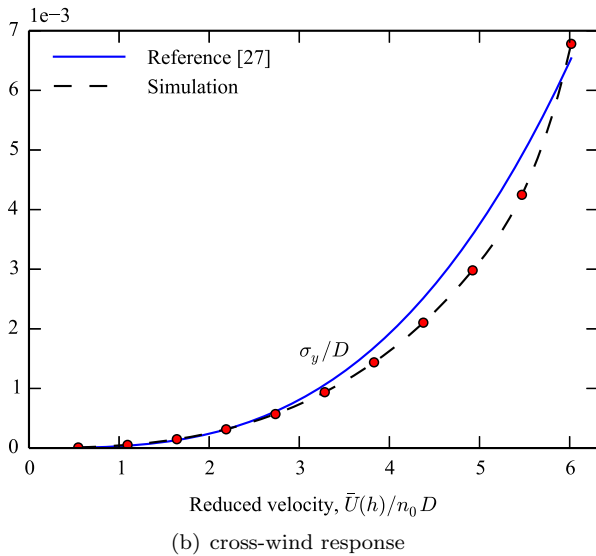
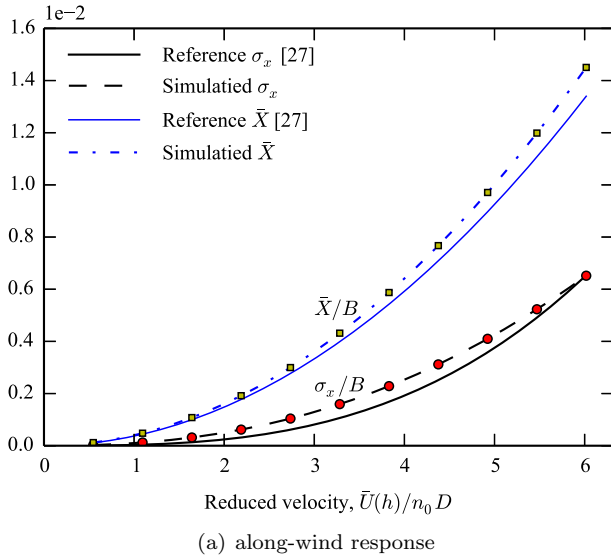


Fig. 4. Comparison between simulated response of the CAARC building and wind tunnel test results [27]; D building depth, B building width, n_0 first-mode frequency, σ_i RMS response in i direction, $i = (x, y)$, μ_x mean response in along-wind direction.

is a primary performance indicator. From the theoretical point of view, vector resultant is not as simple as modal superposition. Therefore, combination rules such as CQC or SRSS are not a valid option in this case [39]. Starting from probability theory, alternative methods have been proposed and utilized to compute peak value of non-Gaussian process, such as the translation process model, the Hermite moment model and the vector process model.

In the special case when the mean responses in the two primary directions (x, y) are both zero and the RMS responses in the two directions are the same, the Rayleigh distribution is an adequate model to describe resultant responses; details are in [38,39].

In this study, the translation process model is employed to investigate the peak value of the resultant response. Translation process model assumes that the mean up-crossing rate $v(r)$ can be estimated exactly when $r(t)$ (r can be resultant displacement or acceleration) is regarded as a translation process, found by memoryless transformation from a standard Gaussian process $G(t)$ [39] as:

$$r(t) = F_r^{-1}[\Phi(G(t))] \quad (16)$$

in which F_r is the CDF of $r(t)$ and F_r^{-1} is its inverse function; Φ is the CDF of the standard normal distribution.

Then, the peak value of $r(t)$ is

$$r_{\max} = F_r^{-1} \left[\Phi \left(\beta + \frac{0.5772}{\beta} \right) \right] \quad (17)$$

where $\beta = \sqrt{2 \ln v(r)T}$; and $v(r) = \sigma_r / (2\pi\sigma_r)$.

Therefore the first step in the above method is constructing the function F_r , the CDF of $r(t)$.

Serviceability limit state is based on a structure preserving elastic response during vibration caused by wind. The anticipated levels of vibration in the primary lateral resisting force system are sufficiently small to ensure that the response can still be linear. Nonlinear response analysis would be needed in the case of ultimate limit states. Therefore, in this case the processes $r_x(t)$ and $r_y(t)$ can be considered as of Gaussian type [36]. The marginal PDF of $r_x(t)$ and $r_y(t)$ are

$$f(r_i; \mu_{r_i}, \sigma_{r_i}) = \frac{1}{\sigma_{r_i} \sqrt{2\pi}} e^{-\frac{(r_i - \mu_{r_i})^2}{2\sigma_{r_i}^2}} \quad (18)$$

where $i = x, y$ and μ is expectation and σ is standard derivation. As a result, from the assumption that the response in the along-wind and crosswind directions are not correlated, the joint PDF of $r_x(t)$ and $r_y(t)$ is

$$f(r_x, r_y; \mu_{r_x}, \sigma_{r_x}, \mu_{r_y}, \sigma_{r_y}) = \frac{1}{\sigma_{r_x} \sigma_{r_y} 2\pi} e^{-\frac{1}{2} \left[\frac{(r_x - \mu_{r_x})^2}{\sigma_{r_x}^2} + \frac{(r_y - \mu_{r_y})^2}{\sigma_{r_y}^2} \right]} \quad (19)$$

The probability of the resultant response r is the probability “summation” extended to all the points, which satisfy $r^2 = r_x^2 + r_y^2$, expressed as $f_r(r) = \sum f(r_x, r_y | r^2 = r_x^2 + r_y^2)$. In other words, the PDF of r is the line integral of the joint PDF $f(r_x, r_y)$ on a circular path, whose radius is r , shown in Fig. 5. More formally, the PDF of r can be written as

$$\begin{aligned} f_r(r) &= \oint_{\{C: r^2 = r_x^2 + r_y^2\}} f(r_x, r_y) d\vec{s} \\ &= \oint_{\{C: r^2 = r_x^2 + r_y^2\}} \frac{1}{\sigma_{r_x} \sigma_{r_y} 2\pi} e^{-\frac{1}{2} \left[\frac{(r_x - \mu_{r_x})^2}{\sigma_{r_x}^2} + \frac{(r_y - \mu_{r_y})^2}{\sigma_{r_y}^2} \right]} d\vec{s} \end{aligned} \quad (20)$$

The CDF of r is the integral of Eq. (20):

$$F_r(R) = P(r \leq R) = \int_0^R f_r(r) dr \quad (21)$$

Estimation of the integrals in Eqs. (20) and (21) can be carried out numerically in an efficient way, since closed-form solution is only available in a limited number of cases [39]. For example, in the previous section and in the case of the CAARC model, when $\bar{U}(h) = 50$ m/s, the mean along-wind displacement $\mu_x = 0.366$ m, mean crosswind displacement $\mu_y = 0$, RMS along-wind displace-

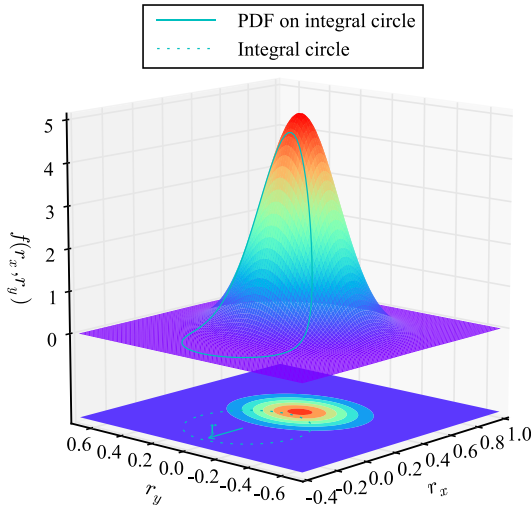


Fig. 5. Joint probability distribution $f(r_x, r_y)$ and integral path $C: r^2 = r_x^2 + r_y^2$.

ment $\sigma_x = 0.160$ m, RMS crosswind displacement $\sigma_y = 0.194$ m, RMS along-wind velocity $\sigma_{\dot{x}} = 0.149$ m/s and RMS crosswind velocity $\sigma_{\dot{y}} = 0.225$ m/s. The joint probability distribution and line integral on circular path are demonstrated in Fig. 5. Calculated from Eq. (20), the resultant displacement PDF $P(r_d)$ and CDF $F_{r_d}(r_d)$ are shown in Fig. 6.

From Fig. 6, the expectation and standard deviation of resultant displacement r_d can be deduced: $E(r_d) = 0.417$ m, $\sigma_{r_d} = 0.152$ m. Repeating the above procedure, the standard deviation of resultant velocity is calculated as $\sigma_{\dot{r}_d} = 0.129$ m/s. According to Eq. (17), the peak values of the resultant displacement are $v(r_d) = \sigma_{\dot{r}_d} / (2\pi\sigma_{r_d}) = 0.136$, $\beta = 2.967$, $r_{d,\max} = 0.913$ m. This method can be applied to building acceleration in the same manner, $\sigma_{r_a} = 0.158$ m/s², $r_{a,\max} = 0.977$ m/s². The σ_{r_a} and $r_{d,\max}$, which are utilized as the performance indicators for serviceability limit states are plotted in Fig. 7.

4.4. Fragility analysis: simulations and numerical results

The basic idea of the Monte Carlo simulation relies on the repeated and independent evaluation of each random input set.

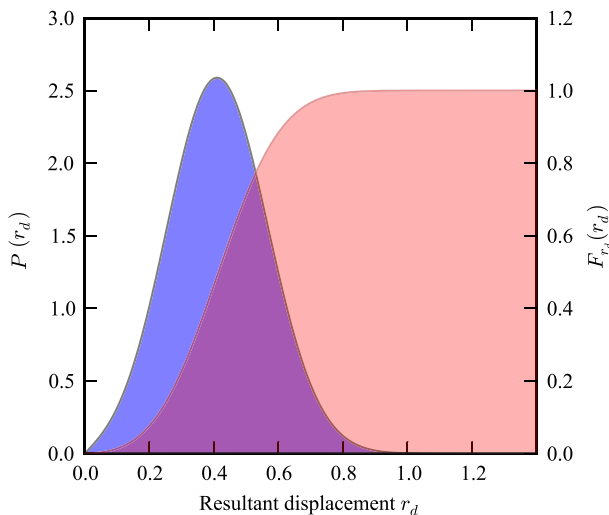


Fig. 6. Probability distribution function (PDF) $P(r_d)$ and cumulative distribution function (CDF) $F_{r_d}(r_d)$ of resultant displacement.

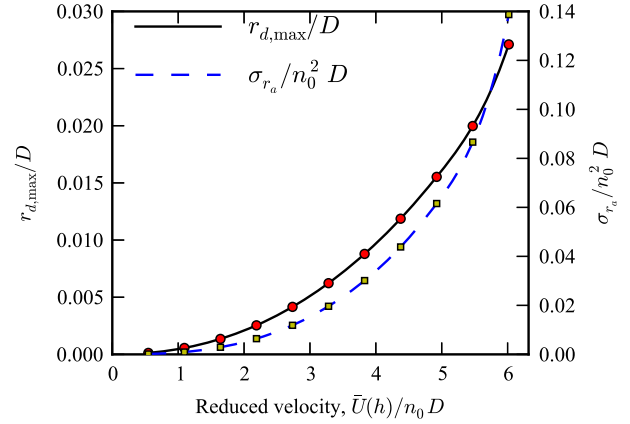


Fig. 7. Simulated peak resultant displacement and RMS resultant acceleration; r_d resultant displacement, σ_{r_a} resultant acceleration.

In this study, the effects of the random drag coefficient C_D , the derivative of lift coefficient $\frac{\partial C_L}{\partial \alpha}$ and the RMS lift coefficient \tilde{C}_L for vortex shedding are analyzed. The randomization of these parameters emulates the contamination associated with measurement errors during wind tunnel experiments described in [27]. The properties of the three random variables are summarized in Table 3. As outlined in the introduction, uncertainty arising from other aerodynamic coefficients (e.g., coherence coefficient C_z) and other sources related to structural properties (e.g., structural damping and structural frequency) are not included.

Figs. 8–10 show the probability density function (PDF) of the random aerodynamic coefficients described in Table 3, and the histograms obtained from the numerical generation of pseudo-random variables [54]. The total number of realizations (sample size) \mathcal{N} is 5000, which is large enough to perform adequate fragility analysis [2,21]. In Figs. 8–10, the occurrences in each bin of the histograms are normalized, which means the total area of a histogram is always normalized to 1.

Figs. 11 and 12 illustrate the Monte Carlo simulation results when the wind velocity is $\bar{U}(h) = 32$ m/s (reduced velocity $\bar{U}(h)/n_0 D = 5.25$ compatible with the experiments in [27]). Histograms in both figures roughly show the probability density distribution. Fig. 11 shows the PDF of top-floor peak resultant displacement, and Fig. 12 depicts the PDF of top-floor RMS resultant acceleration.

As expected, since three random coefficients with different distribution models are involved in this simulation, the response PDFs are not simple gamma-type or other distributions, related to the random input. Therefore, the maximum likelihood method is applied to determine a suitable probabilistic distribution model, fitting the simulated results. For each hypothetical probabilistic model, the Kolmogorov–Smirnov test [55,56] is used to assess the “best distribution model” with a level of significance of 5%. The test results are outlined in Table 4, where the p -value is an indicator of the goodness of hypothetical probabilistic model in range [0,1]; a small p -value implies a doubt on the validity of the tested probabilistic model in comparison with the simulated data.

Table 3
Parameters of random coefficients.

Coefficient	Type	Expectation, μ	Standard deviation, σ
C_D	Gamma	1.54	0.5
$\frac{\partial C_L}{\partial \alpha}$	Normal	−3.5	0.5
\tilde{C}_L	Gamma	0.2870	0.02

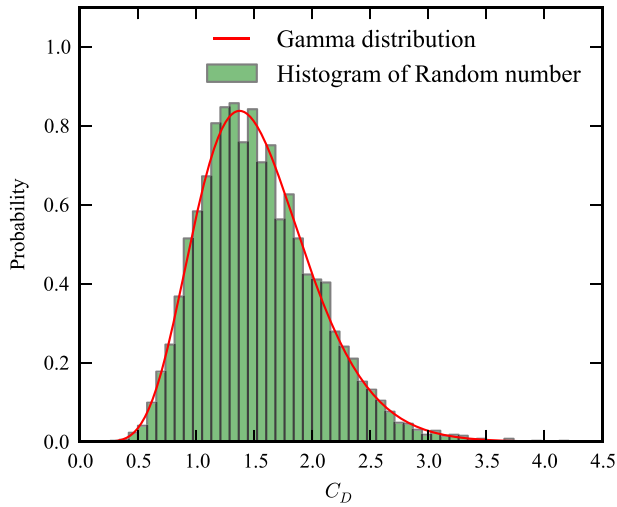


Fig. 8. Gamma-type random distribution of the drag coefficient C_D .

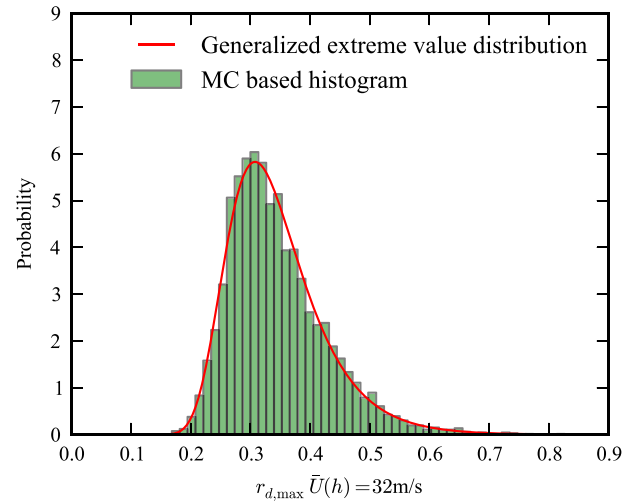


Fig. 11. Distribution of MC simulated results for $\bar{U}(h) = 32$ m/s (peak resultant displacement, $r_{d,max}$).

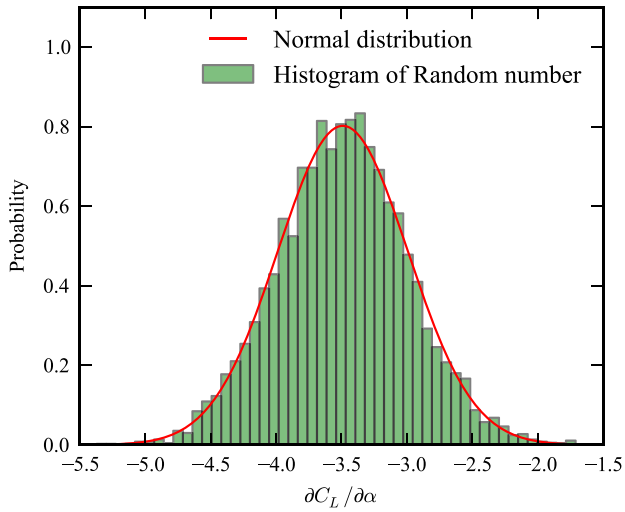


Fig. 9. Normal-type random distribution of the derivative of lift coefficient $\partial C_L / \partial \alpha$.

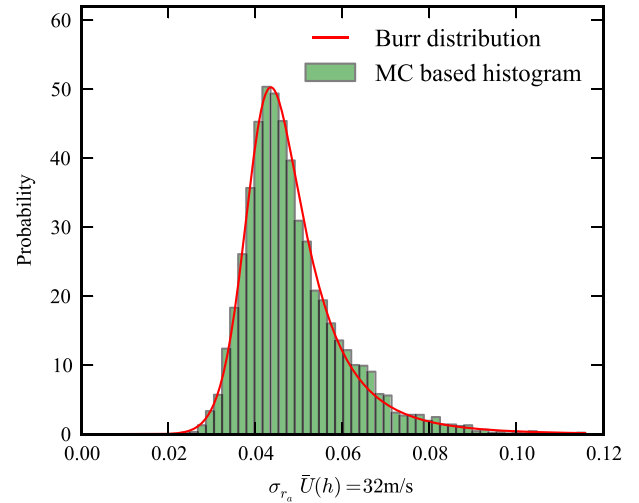


Fig. 12. Distribution of MC simulated results for $\bar{U}(h) = 32$ m/s (RMS resultant acceleration, σ_{ra}).

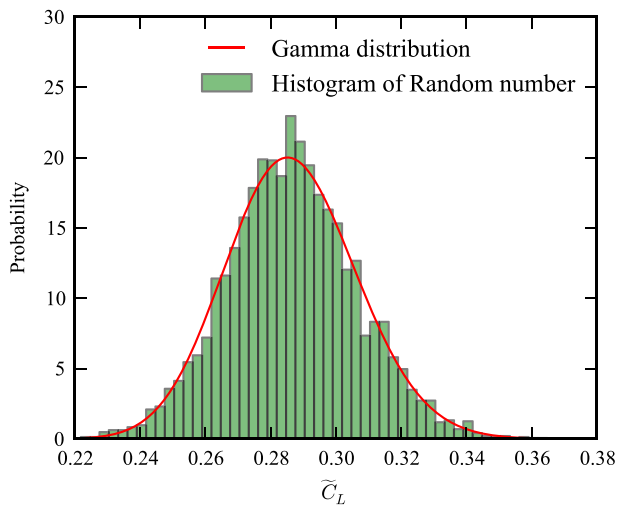


Fig. 10. Gamma-type random distribution of the RMS lift coefficient \bar{C}_L .

Table 4

Kolmogorov–Smirnov results.

Peak displacement, $r_{d,max}$			RMS acceleration, σ_{ra}		
Model	Result	p -value	Model	Result	p -value
Normal	Rejected	1.74×10^{-27}	Normal	Rejected	1.67×10^{-49}
Log-normal	Rejected	1.90×10^{-6}	Log-normal	Rejected	3.08×10^{-17}
Gamma	Rejected	1.34×10^{-11}	Gamma	Rejected	1.22×10^{-26}
Weibull	Rejected	3.88×10^{-37}	Weibull	Rejected	4.56×10^{-55}
Burr	Rejected	4.9×10^{-2}	Burr	Pass	0.0579
GEV ^a	Pass	0.4216	GEV ^a	Rejected	0.0026

^a GEV denotes generalized extreme value distribution.

The Kolmogorov–Smirnov test will reject the model if it has p -value smaller than 5%.

In Table 4, a generalized extreme value (GEV) distribution is used to describe the various probabilistic distribution models with the density function:

$$f_{GEV}(x; \mu, \sigma, \xi) = \frac{1}{\sigma} \left[1 + \xi \left(\frac{x - \mu}{\sigma} \right) \right]^{(-1/\xi)-1} e^{-[1 + \xi \left(\frac{x - \mu}{\sigma} \right)]^{-1/\xi}} \quad (22)$$

The GEV distribution is a family of continuous probability distributions developed within extreme value theory to combine the Gumbel, Fréchet and Weibull families [57]. This distribution allows the data to “choose” which extreme value distribution model is appropriate [56]. The curve with continuous line “—” in Fig. 11 is the GEV fitting result for peak resultant displacement, and the three parameters’ values are $\mu = 0.3082$, $\sigma = 0.0631$, $\xi = 0.0032$.

For the RMS resultant acceleration, a Burr distribution [58] is selected as the most appropriate model to describe the numerical results. The PDF of the Burr distribution is

$$f_{\text{Burr}}(x; c, k) = ck \frac{x^{c-1}}{(1+x^c)^{k+1}} \quad (23)$$

This probabilistic model comes from a very flexible distribution family with two parameters that can express a wide range of distribution shapes; it is capable to fit a wide range of empirical data. In Fig. 12, when $c = 11.70$, $k = 0.4817$, the Burr distribution agrees very well with the simulated results.

After synthesizing all the simulated results for random aerodynamic coefficients when the wind velocity $\bar{U}(h)$ is in the range between 20 m/s and 50 m/s, the fragility curve is plotted in Fig. 13 for the following predefined thresholds: the limit state for the peak lateral displacement (drift) at the top floor is $h/400 = 0.46$ m and limit state for RMS acceleration is 5 mg (0.049 m/s^2). The curve in Fig. 13 connect the simulated points by “Piecewise Cubic Hermite Interpolating Polynomial” [59] (C^1 continuity).

Fig. 13 is divided into three regions. In Region I the vulnerability for all limit states is approximately zero; in Region III vulnerability for all limit states is nearly 1; while in region II, the vulnerability varies from 0 to 1, which means that in this region the wind-induced structural damage is probabilistic rather than deterministic.

4.5. Estimation of wind speed probability density function

As stated in Section 2.5, wind speed probability distribution in a hurricane-prone region should include both hurricane and non-hurricane winds. In order to simulate the vulnerability of a tall building in the Miami area (Florida, United States), the non-hurricane wind speed data are taken from a meteorological coastal station in the proximity of the site (NOAA station No. MLRF1) [60]. This station is located at the south tip of Florida; its coordinates are (25.012N, 80.376W); the station is part of the National Oceanic

and Atmospheric Administration (NOAA) system. Wind Speed is recorded by an anemometer at $z_{g,s} = 11.3$ m above the mean sea level. The wind speed data provided from the database of NOAA are ten-minute averages. The data are converted to the 10-min wind speed at 183 m (the height of CAARC building) by Eqs. (24)–(26) [37].

$$\bar{U}(z_{g,s}, z_{0,s}) = 2.5u_s^* \ln \frac{z_{g,s}}{z_{0,s}} \quad (24)$$

$$\bar{U}(h, z_0) = 2.5u^* \ln \frac{h}{z_0} \quad (25)$$

$$\frac{u^*}{u_s^*} = \left(\frac{z_0}{z_s} \right)^{0.0706} \quad (26)$$

where land roughness $z_0 = 0.5$ m and sea surface (NOAA station) roughness $z_{0,s} = 0.002$ m; and u^* and u_s^* are the shear velocity on land and sea respectively.

For non-hurricane climate, the probability distribution curves in Fig. 14 are evaluated by fitting the Gumbel distribution model to 12 years of annual wind speed maxima records from NOAA. The hurricane wind speed distribution model is assumed to be of Weibull type [37]. The CDF and PDF of wind speed distribution in mixed climate are calculated from Eqs. (9) and (10). The results, plotted in Fig. 14, show that in the hurricane prone region (e.g., South Florida, Gulf of Mexico) hurricane climate dominates the local annual-maxima wind speed, since CDF and PDF of hurricane wind distribution and mixed wind distribution are almost identical.

4.6. Simulation of life-time intervention costs

Table 5 shows the probabilities of each limit state according to each threshold and Eq. (12).

The values of relative cost ϵ_j in Eq. (12) were based on simple considerations on the severity of each damage scenario. For example, the cost ϵ_1 for large lateral deformation damage could be interpreted as the need for intervention on 10% of the cladding elements on the facade of the building. In the case of ϵ_2 for the comfort to the occupant the “maintenance cost” could be estimated as equivalent indirect losses in the business activities due to the temporary interruption of the work in an office; this hypothesis might also include the “internalization of external costs”, i.e., the “ripple effects” produced by losses to businesses and other industries. The value of ϵ_2 is assumed to be 0.2. A time projection

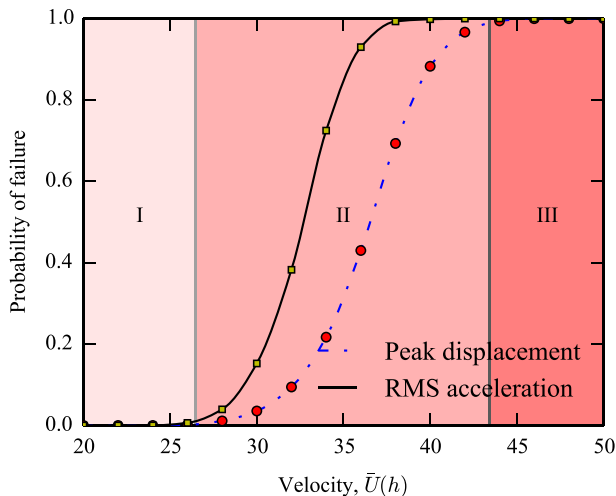


Fig. 13. Example of fragility curve as a function of $\bar{U}(h)$.

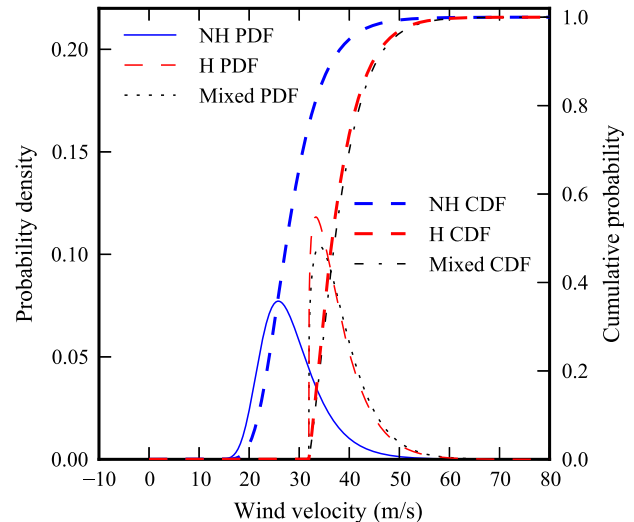


Fig. 14. PDF of annual maxima wind velocity.

Table 5Probability of limit states P_j in Eq. (12) based on the thresholds T_j .

Limit state no. and type	Threshold	P_j
1 (Peak displacement)	0.4575 m	0.5491
2 (RMS acceleration)	0.0049 m/s ²	0.8563

of 50 years or 100 years was used with a five percent discount rate $\lambda = 5\%$ per year [28].

The parameter κ of the Poisson process $N(t)$ in Eq. (12) i.e., the annual occurrence rate of wind hazards, is defined as the recurrence time of the minimum velocity that has non-zero fragility for at least one of the limit states, as

$$\kappa = 1 - F_m \left[\min \left(v_{|F_{T_j}(v) > 0, \forall i} \right) \right] \quad (27)$$

For the CAARC model, based on the results from the previous sections, the annual wind hazard occurrence rate is $\kappa = 1.0$ (i.e., on average at least one high-wind event per year). After combining the annual structural damage probability P_j , annual wind hazards occurrence rate μ , relative repair cost ϵ_j and discount rate λ , the

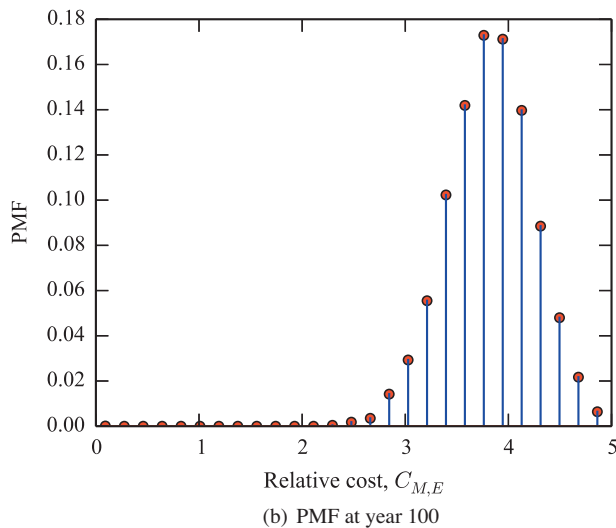
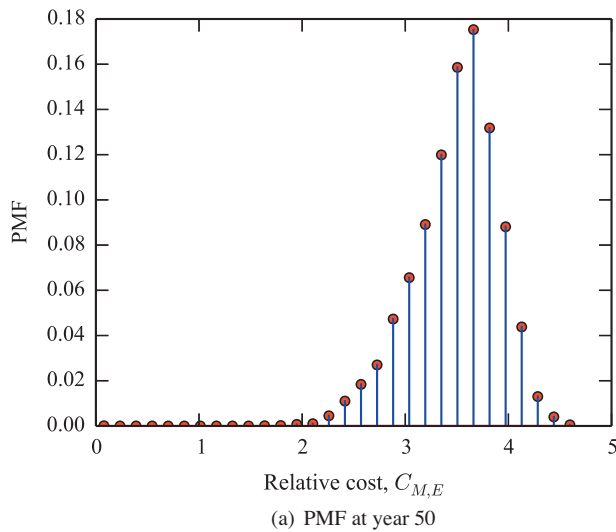


Fig. 15. Probability mass function (PMF) of relative intervention costs (maintenance and repair) normalized to the initial construction cost.

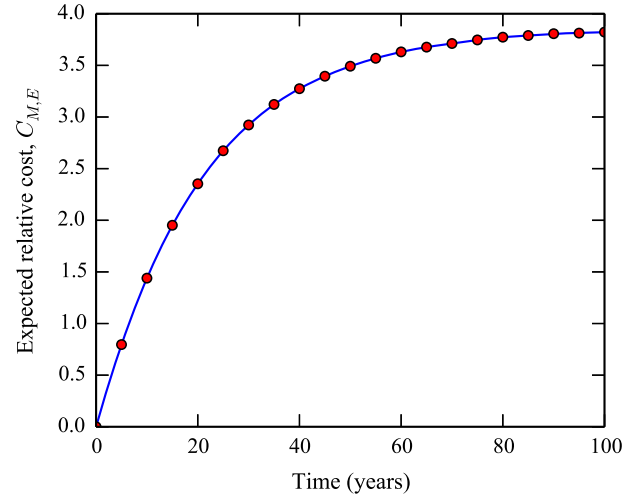


Fig. 16. Expected relative intervention costs (maintenance and repair) normalized to the initial construction cost.

structural life-time relative cost $C_{M,E}$ is simulated and plotted in Figs. 15 and 16.

In the structural life-time, the arrival time of the wind hazards (t_i in Eq. (12)) is considered as a uniform process between 0 and t . Monte-Carlo sampling is used to simulate the series t_i in Eq. (12). The concept of probability mass function (PMF) is utilized to describe how the cost distributes during life-time. Fig. 15 illustrates the PMF of the relative intervention costs $C_{M,E}$ (maintenance and repair) using 10,000 repeated simulations when the building's design life-time is 50 years and 100 years. As the structural life-time grows, the progressive accumulation of normalized expected maintenance and repair costs is plotted in Fig. 16. Because of the effect of discount rate λ , in the later period of structural life-time, the projected cost will only marginally increase (e.g., beyond 80 years in Fig. 16).

5. Life-time cost result and discussion

Estimation of structural life-time cost is influenced by various factors, such as selection criteria for the limit-states, geographical location (different wind climates) and variability in the measurement and estimation of structural and aerodynamic parameters. In the following sections a parametric investigation is carried out to discuss the influence of these factors on structural life-time cost.

5.1. RMS vs. peak for acceleration limit state

For the serviceability, the selection of acceleration limit state criteria, RMS or peak acceleration, can significantly affect structural fragility and subsequent life-time cost estimation. For the occupant comfort criterion, 20 mg has been proposed as the human tolerance threshold (peak acceleration) to be used for the structural design [8]. Using the same simulation procedure from Eqs. (1)–(8), the fragility curve for 20 mg peak resultant acceleration is plotted in dashed line in Fig. 17 and compared to the fragility curve for 5 mg RMS resultant acceleration, which has been selected earlier in this study. From the analysis of Fig. 17 it is noted that 20 mg peak acceleration is a far more strict design criterion than 5 mg RMS acceleration. For example, when the mean wind velocity is $\bar{U}(h) = 30$ m/s, the “vulnerability” for 20 mg peak acceleration is 85.7%, while the “vulnerability” for 5 mg RMS acceleration is 15.2%. High wind-induced vulnerability can lead to high damage probability. In the same meteorological environment

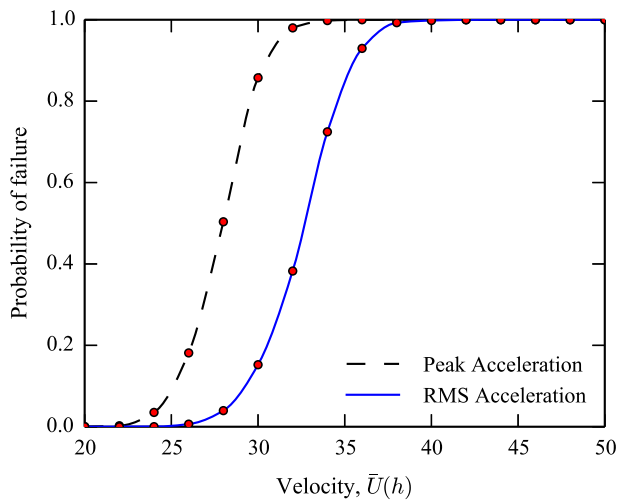


Fig. 17. Fragility curve for RMS-acceleration threshold vs. peak-acceleration threshold.

(same f_m in Eq. (10) from NOAA MLRF1 station), the annual damage probability P_2 in Eq. (13) becomes 0.9976 for 20 mg peak acceleration threshold, which is larger than 0.8563 for the 5 mg RMS acceleration. Higher annual damage probability would yield larger life-time intervention costs according to Eqs. (12) and (11). In Fig. 18, the normalized life-time intervention costs, derived from the two different acceleration limit state criteria, are compared. Because of the much higher P_2 for 20 mg peak acceleration threshold, when the structural life-time is 50 years, the expected normalized cost is 4.05 for 20 mg peak acceleration threshold, while the cost is 3.82 for the 5 mg RMS acceleration threshold, with a relative variation equal to 6.0%.

5.2. Different wind climates

Meteorological environment and different geographical location are important factors in the evaluation of convolution integral and damage probability P_j in Eq. (13).

In addition to the NOAA station MLRF1 located in Southern Florida, the annual-maxima wind data from the NOAA station 46026 (37.755N, 122.839W) near San Francisco in California, USA is also

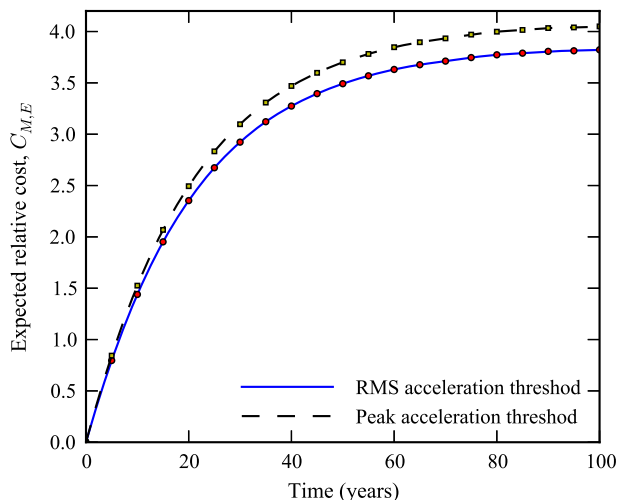


Fig. 18. Comparison between costs employing fragility results either based on RMS-acceleration threshold or peak-acceleration threshold (for occupant comfort).

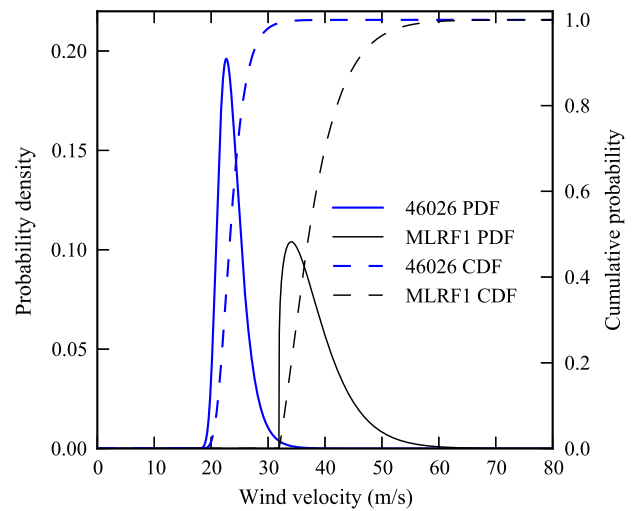


Fig. 19. Comparison of annual-maxima wind speed derived from NOAA 46026 and MLRF1 stations.

employed for cost simulation. Fig. 19 illustrates the comparison of the CDF and PDF of the annual-maxima wind speed in two above locations. Since California is situated on the east shore of the Pacific Ocean, the landing of a hurricane is not possible. As a result, non-hurricane wind climate can be used to adequately analyze wind speed probability in the region of California. Fig. 19 demonstrates that, around the NOAA station 46026, the annual-maxima wind is concentrated in the interval between 10 m/s and 28 m/s, where the vulnerability of CAARC buildings is almost 0. In contrast, in the region near the NOAA station MLRF1, the annual-maxima wind speed is distributed from 32 m/s to 60 m/s; in this interval of

Table 6

Probability of limit states P_j for NOAA 46026 and MLRF1 stations.

Limit state no. and type	Threshold	P_j	
		MLRF1	46026
1 (Peak displacement)	0.4575 m	0.5857	0.0125
2 (RMS acceleration)	0.0049 m/s ²	0.8759	0.0036

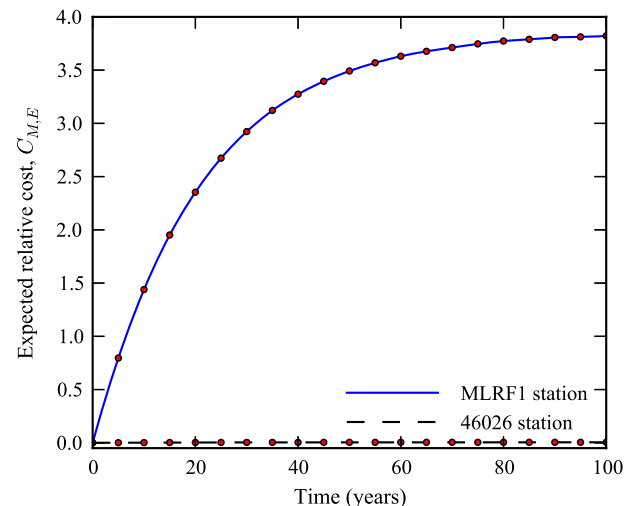


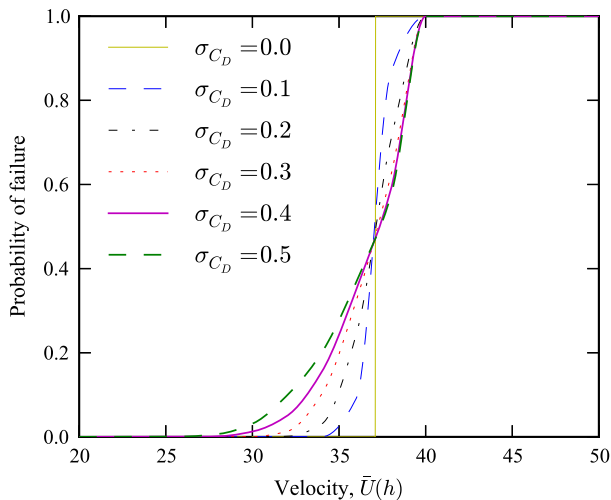
Fig. 20. Comparison of average intervention costs derived from NOAA 46026 and MLRF1 stations.

speeds the vulnerability of CAARC model is much more significant than with the site of the NOAA station 46026.

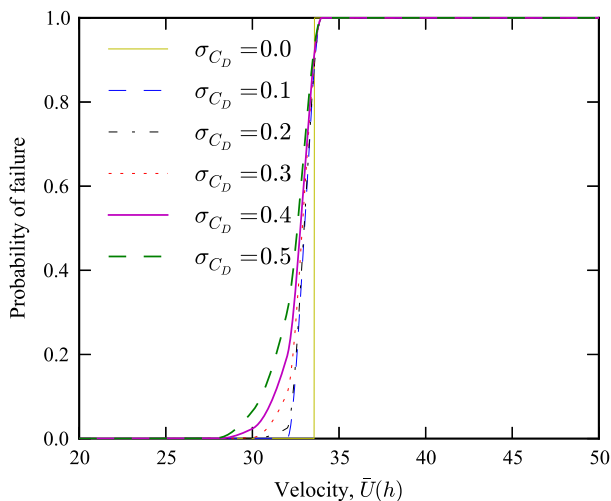
Table 6 lists the annual damage probability for both building locations near NOAA station 46026 and MLRF1. For the NOAA station 46026, the annual-maxima wind probability distribution and the fragility curve marginally interact. The P_j calculated from Eq. (13) is negligible compared to the P_j for NOAA station MLRF1. Similarly, the life-time average intervention cost for the damage on the CAARC building from wind hazards near California is also negligible (10^{-3} of the cost for station MLRF1) in comparison with the cost incurred in the Florida region, shown in Fig. 20.

5.3. Estimation of structural error-contaminated parameters

The standard deviation of aerodynamic coefficients, reflecting the measurement inaccuracy, directly influence the probability distribution of the parameters. As a result, the structural response induced by turbulence is also affected by the standard deviation of the random aerodynamic coefficients. A variation in the standard deviation can modify the shape of the output fragility curve. Larger standard deviation can lead to a wider region of fragility curve, which can in turn increase the annual damage probability, P_j .



(a) Fragility curve for peak displacement limit state



(b) Fragility curve for RMS acceleration limit state

Fig. 21. Comparison of fragility curve with different standard deviations of C_D .

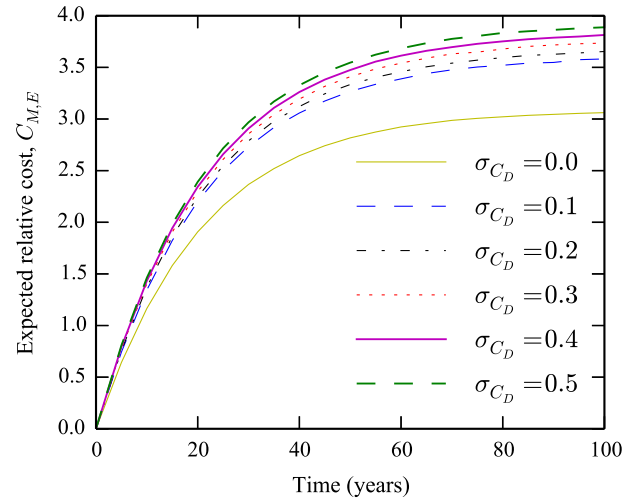


Fig. 22. Comparison of life-time costs derived with different standard deviations of C_D .

Fig. 21 compares the fragility for the two limit states, peak resultant displacement (lateral drift) and RMS acceleration, generated by varying the standard deviation of the random drag coefficient C_D from 0.0 to 0.5. The case with zero standard deviation also corresponds to the “deterministic” solution with no uncertainty. The variation of the other parameters ($\frac{\partial C_L}{\partial x}$ and \bar{C}_L) is not included in this parametric investigation. In the case of the peak displacement limit state, larger σ_{C_D} standard deviations result in “flatter” curves. For the RMS acceleration limit state, the fragility curve exhibits a similar phenomenon.

Variation in the fragility curves can produce different life-time costs as depicted in Fig. 22. For example, in Fig. 22, the normalized life-time cost at 100 years when $\sigma_{C_D} = 0.5$ is 3.86, which is 8.2% larger than the cost when $\sigma_{C_D} = 0.1$ and 27.2 % larger than the cost when $\sigma_{C_D} = 0.0$ (no errors). It is reasonable to suggest that with the development of advanced wind tunnel test technologies and structural dynamic theory, the uncertainty in the aerodynamic coefficients will decrease and, therefore, the building’s budget for life-time repair and maintenance might be reduced.

6. Conclusions

A Monte-Carlo-based procedure was presented for predicting the structural life-time intervention costs of a tall building due to wind-induced damage. A 183 m tall building was employed in this study as the prototype structure. The effect of experimental errors in the measurement of the input aerodynamic load coefficients, derived from the literature, was investigated.

The structural dynamic response in the two principal directions (along-wind and crosswind), induced by turbulent wind, was derived by standard frequency domain analysis method. The lateral drift, accounting for the contribution of both along-wind and crosswind response components, was derived from path integration performed on the joint probability distribution of the response in the two principal directions. The peak value of the lateral drift, which is a non-Gaussian process, was adequately estimated by translation process theory. This numerical approach analyzed the evaluation of fragility curves of both peak lateral drift limit state and RMS acceleration limit state at the top-floor of the structure. This information was used to evaluate the vulnerability of the structure to predefined thresholds for each limit state due to wind hazard. A life-cycle cost analysis algorithm was also developed,

which estimates the intervention costs (repair and maintenance) using the results of the fragility analysis.

The numerical results of this paper demonstrate that the proposed approach could be used for evaluating life-cycle intervention costs of the structure; it can potentially be used for performance-based design of tall buildings [61]. The cost analysis results also suggest that, as the hazard exposure time increases, the cost will tend to a limit. In the last part of this paper, it is found that the structural life-time cost can be influenced by the selection of various limit states, by the site wind environment and the standard derivation of the error-contaminated aerodynamic load coefficients. The factor that predominantly influences the cost estimation is the local meteorological wind environment, inducing life-time cost with large differences (orders of magnitude). For a region rarely affected by hurricanes in the United States, the life-time intervention costs, caused by wind hazards, is negligible.

Future investigations should account for torsional response caused by buffeting loads and vortex shedding effects. The correlation of crosswind and torsional response should also be carefully considered in the cost analysis, along with wind directionality effects. Finally, other uncertainty sources, may be included in the evaluation of fragility curves, such as building frequencies and structural damping. Furthermore, the framework proposed in this paper may be applied to other types of vertical structures (light poles, chimneys) or secondary structural elements (curtain wall systems, cornices for buildings).

Acknowledgments

This material is based upon work supported by the National Science Foundation (NSF) of the United States under CAREER Award, CMMI 0844977. Any opinions, findings and conclusions or recommendations are those of the authors and do not necessarily reflect the views of the NSF.

References

- [1] SEAOC. Vision 2000: performance based seismic engineering of buildings. Sacramento, California: Structural Engineers Association of California; 1995.
- [2] Smith MA, Caracoglia L. A Monte Carlo based method for the dynamic "fragility analysis" of tall buildings under turbulent wind loading. *Eng Struct* 2011;33(2):410–20.
- [3] Hart GC, Jain A. Performance based wind design of tall concrete buildings in the Los Angeles region utilizing structural reliability and nonlinear time history analysis. In: The 12th Americas conference on wind engineering (12ACWE); 2013.
- [4] Pozzuoli C, Bartoli G, Peil U, Clobes M. Serviceability wind risk assessment of tall buildings including aeroelastic effects. *J Wind Eng Ind Aerodyn* 2013;123(Part B):325–38.
- [5] Bernardini E, Spence S, Giofrè M, Kareem A. A reliability approach for the wind-induced response assessment of tall buildings using the high frequency force balance. In: The seventh international colloquium on bluff body aerodynamics and applications (BBA7); 2012. p. 825–34.
- [6] Spence SM, Giofrè M. Large scale reliability-based design optimization of wind excited tall buildings. *Prob Eng Mech* 2012;28:206–15.
- [7] Bernardini E, Spence SM, Kareem A. A probabilistic approach for the full response estimation of tall buildings with 3d modes using the HFFB. *Struct Saf* 2013;44:91–101.
- [8] Griffis LG. Serviceability limit states under wind load. *Am Inst Steel Constr* 2003.
- [9] Ciampoli M, Petrini F. Performance-based aeolian risk assessment and reduction for tall buildings. *Prob Eng Mech* 2012;28:75–84.
- [10] Unanwa C, McDonald J, Mehta K, Smith D. The development of wind damage bands for buildings. *J Wind Eng Ind Aerodyn* 2000;84(1):119–49.
- [11] Inokuma A. Basic study of performance-based design in civil engineering. *J Prof Issues Eng Educ Pract* 2002;128(1):30–5.
- [12] Ellingwood B, Rosowsky D, Li Y, Kim J. Fragility assessment of light-frame wood construction subjected to wind and earthquake hazards. *J Struct Eng* 2004;130(12):1921–30.
- [13] Ellingwood B, Tekie P. Wind load statistics for probability-based structural design. *J Struct Eng* 1999;125(4):453–63.
- [14] Li Y, Ellingwood BR. Hurricane damage to residential construction in the US: importance of uncertainty modeling in risk assessment. *Eng Struct* 2006;28(7):1009–18.
- [15] van de Lindt J, Dao T. Performance-based wind engineering for wood-frame buildings. *J Struct Eng* 2009;135(2):169–77.
- [16] Barbato M, Petrini F, Unnikrishnan VU, Ciampoli M. Performance-based hurricane engineering (PBHE) framework. *Struct Saf* 2013;45(0):24–35.
- [17] Bashor R, Kareem A. Probabilistic performance evaluation of buildings: an occupant comfort perspective. In: Proceedings of the 12th international conference on wind engineering; 2007. p. 1–6.
- [18] Norton T, Abdullah M, Stephens D. Proposed methodology for performance-based vulnerability assessment of wind-excited tall buildings. In: Fourth international conference on Advances in Wind and Structures (AWAS); 2008. p. 1228–46.
- [19] Jain A, Srinivasan M, Hart GC. Performance based design extreme wind loads on a tall building. *Struct Des Tall Build* 2001;10(1):9–26.
- [20] Seo DW, Caracoglia L. Statistical buffeting response of flexible bridges influenced by errors in aeroelastic loading estimation. *J Wind Eng Ind Aerodyn* 2012;104:129–40.
- [21] Seo DW, Caracoglia L. Estimating life-cycle monetary losses due to wind hazards: fragility analysis of long-span bridges. *Eng Struct* 2013;56:1593–606.
- [22] Davenport AG. The response of six building shapes to turbulent wind. *Philos Trans Roy Soc London Ser A, Math Phys Sci* 1971;269(1199):385–94.
- [23] Davenport AG. The response of supertall buildings to wind. In: Second century of the skyscraper. Springer; 1988. p. 705–25.
- [24] Chen X. Estimation of extreme value distribution of crosswind response of wind-excited flexible structures based on extrapolation of crossing rate. *Eng Struct* 2014;60:177–88.
- [25] Wojtkiewicz SF. Use of GPU computing for uncertainty quantification in computational mechanics: a case study. *Sci Program* 2011;19(4):199–212.
- [26] Bernardini E, Spence SM, Giofrè M. Effects of the aerodynamic uncertainties in HFFB loading schemes on the response of tall buildings with coupled dynamic modes. *Eng Struct* 2012;42:329–41.
- [27] Melbourne W. Comparison of measurements on the CAARC standard tall building model in simulated model wind flows. *J Wind Eng Ind Aerodyn* 1980;6(1):73–88.
- [28] Wen YK, Kang YJ. Minimum building lifecycle cost design criteria. I: Methodology. *J Struct Eng (ASCE)* 2001;127(3):330–7.
- [29] Val DV, Stewart MG. Life-cycle cost analysis of reinforced concrete structures in marine environments. *Struct Saf* 2003;25(4):343–62.
- [30] Frangopol DM, Kong JS, Gharaibeh ES. Reliability-based life-cycle management of highway bridges. *J Comput Civ Eng* 2001;15(1):27–34.
- [31] Piccardo G, Solari G. Generalized equivalent spectrum technique. *Wind Struct* 1998;1(2):161–74.
- [32] Kareem A. Acrosswind response of buildings. *J Struct Divis* 1982;108(4):869–87.
- [33] Dyrbye C, Hansen SO. Wind loads on structures. 1st ed. New Jersey, USA: John Wiley & Sons; 1997.
- [34] Vickery BJ, Clark AW. Lift or across-wind response to tapered stacks. *J Struct Divis* 1972;98(1):1–20.
- [35] Piccardo G, Solari G. 3D wind-excited response of slender structures: closed-form solution. *J Struct Eng (ASCE)* 2000;126(8):936–43.
- [36] Davenport AG. Note on the distribution of the largest value of a random function with application to gust loading. In: ICE proceedings. Thomas Telford; 1964. p. 187–96.
- [37] Simiu E, Scanlan RH. Wind effects on structures: fundamentals and applications to design. 3rd ed. New Jersey, USA: John Wiley & Sons; 1996.
- [38] Huang M, Chan C, Kwok K, Lou W. A peak factor for predicting non-Gaussian peak resultant response of wind-excited tall buildings. In: The seventh Asia-Pacific conference on wind engineering. Taipei, Taiwan; 2009.
- [39] Chen X, Huang G. Evaluation of peak resultant response for wind-excited tall buildings. *Eng Struct* 2009;31(4):858–68.
- [40] Grigoriu M. Crossings of non-Gaussian translation processes. *J Eng Mech (ASCE)* 1984;110(4):610–20.
- [41] Winterstein SR. Non-normal responses and fatigue damage. *J Eng Mech (ASCE)* 1985;111(10):1291–5.
- [42] Belyaev YK. On the number of exits across the boundary of a region by a vector stochastic process. *Theory Prob Appl* 1968;13(2):320–4.
- [43] Chen X, Kareem A. Coupled dynamic analysis and equivalent static wind loads on buildings with three-dimensional modes. *J Struct Eng (ASCE)* 2005;131(7):1071–82.
- [44] Boggs D. Acceleration indexes for human comfort in tall buildings – Peak or RMS; 1997.
- [45] Kwok KC, Hitchcock PA, Burton MD. Perception of vibration and occupant comfort in wind-excited tall buildings. *J Wind Eng Ind Aerodyn* 2009;97(78):368–80 [12th international conference on wind engineering].
- [46] Gomes L, Vickery B. Extreme wind speeds in mixed wind climates. *J Wind Eng Ind Aerodyn* 1978;2(4):331–44.
- [47] Gomes L, Vickery B. On the prediction of extreme wind speeds from the parent distribution. *J Wind Eng Ind Aerodyn* 1977;2(1):21–36.
- [48] Vickery PJ, Wadhera D, Galsworthy J, Peterka JA, Irwin PA, Griffis LA. Ultimate wind load design gust wind speeds in the united states for use in ASCE-7. *J Struct Eng (ASCE)* 2009;136(5):613–25.
- [49] ASCE. Minimum design loads for building and other structures (ASCE 7–10); 2010.
- [50] Batts ME, Simiu E, Russell LR. Hurricane wind speeds in the united states. *J Struct Divis* 1980;106(10):2001–16.
- [51] Vickery PJ, Wadhera D, Twisdale Jr LA, Lavelle FM. US hurricane wind speed risk and uncertainty. *J Struct Eng (ASCE)* 2009;135(3):301–20.

- [52] Kaimal J, Wyngaard J, Izumi Y, Coté O. Spectral characteristics of surface-layer turbulence. *Quart J Roy Meteorol Soc* 1972;98(417):563–89.
- [53] ESDU. Standard 90036: structures of non-circular cross section: dynamic response due to vortex shedding; 2004.
- [54] Moler C. Numerical computing with matlab. MathWorks; 2004.
- [55] Massey Jr FJ. The Kolmogorov–Smirnov test for goodness of fit. *J Am Stat Assoc* 1951;46(253):68–78.
- [56] Mathworks. Matlab documents. Natick, Massachusetts: The MathWorks Inc.; 2013.
- [57] Kotz S, Nadarajah S. Extreme value distributions. Singapore: World Scientific; 2000.
- [58] Tadikamalla PR. A look at the Burr and related distributions. *Int Stat Rev* 1980;48:337–44.
- [59] De Boor C. A practical guide to splines, vol. 27. New York: Springer-Verlag; 1978.
- [60] NOAA. National Data Buoy Center. <<http://www.ndbc.noaa.gov/>>.
- [61] Barbato M, Palmeri A, Petrini F. Special issue on performance-based engineering (editorial). *Eng Struct* 2014;78:1–2.